Quantitative Microwave Imaging of High-Contrast Targets with the Incidence of Orbital Angular Momentum Wave

Shasha Hou[1,2], Kuiwen Xu[1,2,*], Xiaotong Li[3], Feixiang Luo[4], Xiling Luo[4], Sheng Sun[5],
Wenjun Li[1,2], and Lingling Sun[1]

[1] *The Key Lab of RF Circuits and Systems of Ministry of Education, Hangzhou 310018, China*
[2] *Hangzhou Dianzi University, Hangzhou 310018, China*
[3] *The Ceyear Technologies Co., Ltd, Xiangjiang Road, Huangdao District, Qingdao 266555, China*
[4] *Beihang University, Beijing 100190, China*
[5] *School of Electronic Science and Engineering, University of Electronic Science and Technology of China, Chengdu 610056, China*

ABSTRACT: The inherent nonlinearity and ill-posedness of inverse scattering problems (ISPs) make high-quality target reconstruction challenging. To mitigate some of the difficulties and achieve more accurate and stable reconstructions, a super-resolution imaging method by use of the orbital angular momentum (OAM) wave for solving high-contrast targets is proposed. By the interaction of OAM wave and the material of target, the multiple scattering could be enhanced, and more incoherent wave could be activated. Under the frame of the contraction integral equation for inversion (CIE-I) method, the OAM-inspired CIE-I inversion method (OAM-CIE-I) is introduced to achieve super-resolution imaging of high-contrast targets. OAM electromagnetic waves, generated from a two-dimensional uniform circular array (UCA), are used as the incident field into the imaging model. Orbital angular momentum diffraction tomography (OAM-DT) is used to obtain the initial value of the contrast function containing the super-resolution information, which serves as the initial contrast value for the CIE-I model. Despite the initial contrast value differing significantly from the actual target, it contains incoherent wave information, enabling super-resolution imaging through three optimization iterations. In virtue of the inversion solver of the CIE-I, the inversion ability of the OAM-CIE-I is significantly enhanced. In the comparisons from numerical simulation results with CSI, OAM-CSI, CIE, and OAM-CIE methods, the superiority of OAM-CIE-I is demonstrated.

1. INTRODUCTION

Electromagnetic inverse scattering problems (ISPs) involve reconstructing the location, geometric shape, and constitutive parameters (permittivity, permeability, and conductivity) of unknown scattering objects in the domain of interest (DOI) based on the known incident field and scattered field obtained by receivers [1]. ISPs are widely applied in remote sensing [2], petroleum exploration [3], through-wall imaging [4], medical imaging [5, 6], and various other fields. It is well known that solving ISPs faces two major challenges: ill-posedness and nonlinearity [1]. Ill-posedness arises because the number of unknowns to be reconstructed far exceeds the number of measured scattered fields, while nonlinearity is caused by multiple scattering effects within the DOI, which are exacerbated by increases in the relatively high contrast and/or electrically large size of the scatterers.

Inversion methods for solving nonlinear ISPs are typically divided into two types: linear inversion methods and nonlinear iterative methods. Linear inversion methods typically rely on the Born approximation [7]. Owing to neglecting the multiple scattering effects within the DOI. Such linear methods are only applicable to weak scatterers. Nonlinear iterative methods transform the inverse problem into an optimization problem by constructing an objective function and updating parameters

to minimize it, such as contrast source inversion (CSI) [8, 9], Gauss-Newton method [10], and subspace optimization method (SOM) [11].

These inversion methods based on the Lippmann-Schwinger integral equation (LSIE) are suitable for medium scatterers. However, they often encounter challenges when dealing with strong scatterers characterized by high contrast and/or electrically large sizes. To alleviate highly nonlinear ISPs, a new integral equation (NIE) [12] has been proposed. Building upon this integral equation model, the Fourier Bases Expansion with contraction integral equation for inversion (FBE-CIE-I) method [13] has been introduced, effectively suppressing the nonlinearity caused by multiple scattering effects.

Resolution is a key metric for evaluating electromagnetic ISPs. According to the Rayleigh criterion [14], resolution is typically limited by half-wavelength (0.5λ). Recently, orbital angular momentum (OAM) has been applied in the field of imaging to achieve super-resolution imaging. Owing to their orthogonality under different modes, OAM could provide additional known information for electromagnetic ISPs, probably enhancing imaging accuracy and resolution. A super-resolution imaging method based on orbital angular momentum diffraction tomography (OAM-DT) could achieve super-resolution imaging beyond the Rayleigh limit for low-contrast targets [15],

---

* Corresponding author: Kuiwen Xu (kuiwenxu@hdu.edu.cn).

which shed some light on the super-resolution problems with OAM.

This paper focuses on the super-resolution imaging problem of high-contrast targets in frame of the CIE-I model with the OAM wave. The contributions of this work could be summarized as follows:

1. A super-resolution imaging method, OAM-CIE-I, for quantitatively imaging high-contrast targets is proposed. Firstly, the retrieved contrast is obtained using the OAM-DT method, which is then utilized as the initial value for the inversion of the CIE-I. Through multiple rounds of nested inversion schemes, super-resolution imaging of high-contrast targets could be flexibly achieved.

2. Compared to some other imaging methods, the proposed OAM-CIE-I method could achieve better performance of targets with higher contrast by use of several high-order OAM modes.

2. FORWARD PROBLEM MODEL

The basic configuration of the two-dimensional ISPs is illustrated in Fig. 1. In the background of free space with relative permittivity ϵ_0, permeability μ_0, and wavenumber $k_0 = \omega\sqrt{\epsilon_0\mu_0}$, unknown scatterers with relative permittivity ϵ_r are placed within the DOI. Typically, a rectangular area is chosen as the DOI. In practical solving, the DOI is discretized into $M = M_1 \times M_2$ small grid units, with each grid positioned at $r_m = 1, 2, \ldots, M$.
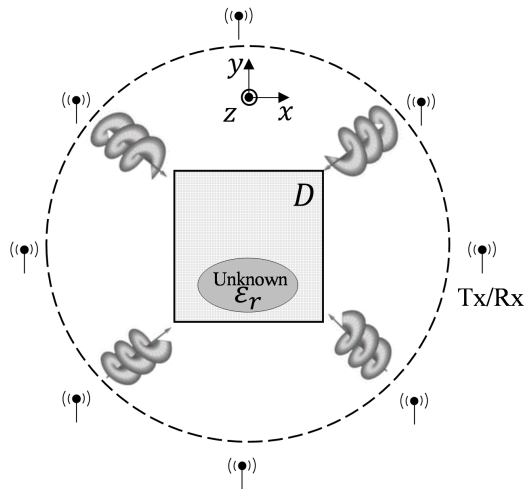

FIGURE 1. Configuration of ISPs with the incidence of OAM wave.

The measurement domain S lies outside the DOI, where N_i transmitting antennas and N_r receiving antennas are uniformly positioned along two circular lines. The transmitting antennas, located at r_p^i, $p = 1, 2, \ldots, N_i$, sequentially illuminate the DOI, while the receiving antennas, located at r_p^s, $p = 1, 2, \ldots, N_r$, collect the scattering field data. The ISPs aim to reconstruct the shape, position, and constitutive parameters of unknown scatterers within the DOI using the collected scattered field data. Based on the two-dimensional LSIE model, the total field E_p^t in the DOI and the scattered field E_p^s on the measurement domain can be written as matrix formulas:

$$\overline{E}_p^t = \overline{E}_p^i + \overline{\overline{G}}_D(\overline{J}_p) \tag{1}$$

$$\overline{E}_p^s = \overline{\overline{G}}_s(\overline{J}_p) \tag{2}$$

where the Green's function $\overline{\overline{G}}_D$ represents the mapping relationship between induced currents and scattered fields in the DOI, and the Green's function $\overline{\overline{G}}_s$ represents the mapping relationship between induced currents in the DOI and measured scattered fields in the measurement domain S. $\overline{J}_p$ is defined as the contrast source. The relationship between the contrast source and total field is denoted as follows:

$$\overline{J}_p = \overline{\overline{\chi}} \cdot \overline{E}_p^t = \overline{\overline{\chi}} \cdot \left(\overline{E}_p^i + \overline{\overline{G}}_D(\overline{J}_p) \right) \tag{3}$$

Combining (2) and (3), we could get the scattered field in the measurement domain.

$$\overline{E}_p^s = \overline{\overline{G}}_s \cdot \left(\overline{\overline{I}} - \overline{\overline{\chi}}\overline{\overline{G}}_D \right)^{-1} \cdot \left(\overline{\overline{\chi}}\overline{E}_p^i \right) \tag{4}$$

Therefore, in the forward model, if the contrast of the scatterers and incidence filed are known, the scattered field could be well obtained by (4). Generally, a linear solver could get the solution [16].

3. HIGH-CONTRAST TARGET SUPER-RESOLUTION IMAGING

Nonlinear methods take into account the multiple scattering effects within the DOI, enabling them to handle moderate scatterers and possess certain super-resolution capabilities. Herein, by utilizing the CIE-I algorithm and OAM electromagnetic waves containing inherent super-resolution information, super-resolution imaging of high-contrast targets could be well achieved, surpassing the performance of both OAM-CSI and CIE-I methods.

3.1. Generating OAM Electromagnetic Waves

To generate OAM electromagnetic waves, various methods can be employed, such as using spiral parabolic antennas [17], spiral phase plates [18], and uniform circular array (UCA) [19]. In this paper, we utilize a UCA to generate two-dimensional OAM electromagnetic waves. As shown in Fig. 1, N antennas are uniformly distributed on a circular ring, with a phase difference of $\delta_\phi = 2\pi L/N$ between adjacent antennas. Here, L represents the topological charge, also known as the mode number of the OAM electromagnetic wave, and the OAM wave could be represented as,

$$E(\rho) = \sum_{n=1}^{N} H_0^2 \left(k_0 |\rho - \rho_n| \right) e^{jLn\delta_\phi} \tag{5}$$

here, ρ_n represents the location of the nth antenna. The uniform circular array consists of 30 antennas, with a radius of 3λ for the circular array. As shown in Fig. 2, the amplitude distribution and phase distribution of OAM electromagnetic waves are
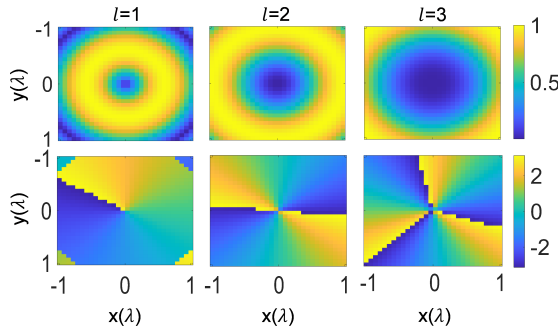
FIGURE 2. Amplitude (first row) and phase distribution (second row) of OAM electromagnetic waves, from left to right $l = 1, 2, 3$.

provided for $L = 1, 2, 3$. It can be observed that a prominent characteristic of OAM electromagnetic waves is their amplitude distribution resembling a "doughnut" shape; as the mode number L of OAM electromagnetic waves increases, the energy voids within the "doughnut" structure become more pronounced. The phase of OAM electromagnetic waves exhibits periodic variations, with the mode number L representing the number of phase cycles.

3.2. OAM-CIE-I Super-Resolution Imaging

By designing the incident field of OAM electromagnetic waves, the incoherent wave information could be turned into the transmitted wave to some extent. The OAM-DT [13] algorithm based on the Born approximation (BA) is only suitable for low-contrast targets.

To achieve high-contrast target imaging, the results of OAM-DT algorithm could be used as initial values in the next step. In this case, under the OAM electromagnetic wave, the scattered field with the BA could be effectively expressed as:

$$E_s = k_0^2 \int_s g(r, r') \cdot \chi E^i \, dr'$$

$$= k_0^2 \int_s g(r, r') \cdot \chi \cdot H_0^2(k_0|\rho - \rho_n|) e^{jln\delta_\phi} \, dr' \qquad (6)$$

which could be written as matrix formulas:

$$\overline{\overline{E}}^s = \overline{\overline{A}}\overline{\overline{\chi}} \qquad (7)$$

To illuminate the targets with multiple modes, let the mode of the OAM electromagnetic wave be denoted as $l = 0, \pm 1, \pm 2, \pm 3, \ldots \pm L$. $\overline{E}_l^s$ denotes the scattered field resulting from the superposition of multiple modes, $\overline{E}_l^s = [E_{-L}^s \ldots E_{-1}^s, E_0^s, E_1^s \ldots E_L^s]$, and $\overline{\overline{A}}$ is the corresponding coefficient matrix $A = [A_{-L} \ldots A_{-1}, A_0, A_1 \ldots A_L]$. Tikhonov regularization technique is used to solve $\overline{\overline{\chi}}$,

$$\overline{\overline{\chi}} = \left(\overline{\overline{A}}^* \cdot \overline{\overline{A}} + \alpha \overline{\overline{I}}^* \cdot \overline{\overline{I}} \right)^{-1} \cdot \overline{\overline{A}}^* \cdot \overline{\overline{E}}^s \qquad (8)$$

here, $\overline{\overline{I}}$ represents the M-order identity matrix, "*" the conjugate transpose, and α the regularization parameter. To reduce the nonlinearity in ISPs modeling for strong scatterers,

a new type of CIE-I was proposed in [10]. Both sides of Equation (3) are multiplied by the modified contrast $\overline{\overline{R}}(r) = \overline{\overline{\beta}}(r)\overline{\overline{\chi}}(r) \cdot (\overline{\overline{\beta}}(r)\overline{\overline{\chi}}(r) + 1)^{-1}$ resulting in the contraction integral equation:

$$\overline{\overline{\beta}} J_p = \overline{\overline{R}} \cdot \left[\overline{\overline{\beta}} J_p + E_p^{inc} + \overline{\overline{G}}_D \cdot J_p \right] \qquad (9)$$

where β is a constant matrix with dimensions $M_1 \times M_2$ and has positive real parts and non-negative imaginary parts. Eqs. (4) and (9) are referred to as the new data equation and state equation, respectively, in the CIE-I model. In order to stabilize the CIE-I model, we adopt the Fourier basis expansion contraction integral equation inversion (FBE-CIE-I) method proposed in [11]. In FBE-CIE-I, the induced current can be expanded by the discrete Fourier bases, and for convenience, 2-D discrete inverse Fourier transform is denoted as F_T^*. The contrast source could be stated in operator form:

$$\overline{J}_p = F_T^*(\overline{\alpha}_p) \qquad (10)$$

Then the contrast source can be represented as:

$$f\left(\overline{\alpha}_1, \overline{\alpha}_2, \ldots \overline{\alpha}_p, \overline{\overline{R}}\right) = \sum_{p=1}^{N_i} \left[\frac{||\triangle_p^{fie}||^2}{||\overline{E}_p^{sca}||^2} + \frac{||\triangle_p^{cur}||^2||^2}{||\overline{E}_p^{inc}||^2} \right] \qquad (11)$$

where $\triangle_p^{fie}$ and $\triangle_p^{cur}$ are the residual of data Equation (4), and object Equation (9) of CIE-I modeling can be defined as:

$$\triangle_p^{fie} = \overline{E}_p^{sca} - F_T^*(\overline{\alpha}_p) \qquad (12)$$

$$\triangle_p^{cur} = \overline{\overline{R}} \cdot \left(\overline{E}_p^{inc} + \overline{\overline{G}}_D \cdot F_T^*(\overline{\alpha}_p) \right) - \left(\overline{\overline{\beta}} - \overline{\overline{R}} \cdot \overline{\overline{\beta}} \right) \cdot F_T^*(\overline{\alpha}_p) \qquad (13)$$

In the inversion process, we alternately utilize the conjugate gradient method and least squares method to update the contrast source and modified contrast function [13]. We employ multiple rounds of nested inversion with different subspace sizes to reconstruct the unknown target. In each optimization round, different values of M_F and β are chosen for optimization.

Physically, due to the orthogonal characteristic of different waves and phase information, the interaction between the OAM wave and target is profoundly full. The utilization of the Born approximation includes the term corresponding to the OAM incident field in matrix A in Equation (7). Compared to the plane wave, more scattered incoherent electromagnetic waves information is convolved by the OAM wave incident field. Mathematically, in order to obtain the more accurate scattered wave information, the regularization technique is used to solve the contrast χ_0 by Equation (8).

3.3. Numerical Simulation

In this section, the DOI is selected as a rectangular region of $2\lambda \times 2\lambda$, with a grid resolution of $2\lambda/30$. 30 transmitting antennas are uniformly placed along a circle with the origin as the center and a radius of 3λ. The scattering field is measured at the same positions. OAM electromagnetic wave illumination mode

is $l = 0, \pm 1, \pm 2, \pm 3, \ldots \pm L$, with the operating frequency of Terahertz wave, i.e., 110 GHz.

In the first example, two uniform rectangular targets with the side lengths of $\lambda/2$ and a boundary distance of $\lambda/4$ are used, as illustrated in Fig. 3(a), with the relative permittivity of $\epsilon_r = 2.0$. Fig. 3(b) displays the reconstructed results by the CSI, which successfully reconstructs the targets. When increasing the relative permittivity of the targets from 2.0 to 3.5, the CSI fails to retrieve the targets as depicted in Fig. 3(c). In such cases, the OAM-CSI is employed for reconstruction, illustrated in Figs. 3(d), (e), (f), with an OAM electromagnetic wave incident mode selected as $L = 7, 9, 11$, respectively. As the number of OAM wave mode is increased, the targets are gradually retrieved, and the resolution is increasing. When the OAM wave mode is chosen as $L = 11$, the OAM-CSI method could effectively reconstruct the targets.
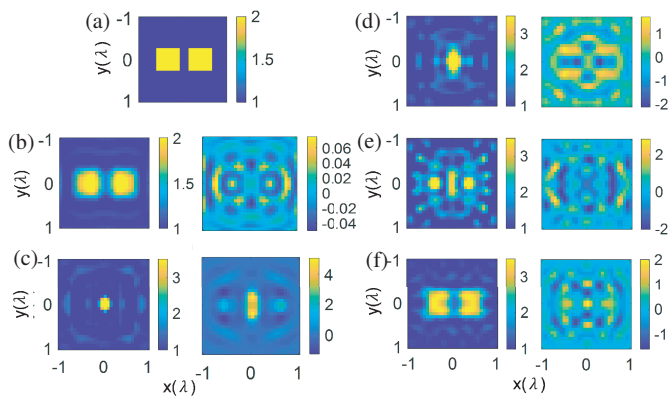

FIGURE 3. Reconstruction results obtained by CSI and OAM-CSI. (a) The ground truth. (b) CSI reconstruction results with $\epsilon_r = 2.0$. (c) CSI reconstruction results with $\epsilon_r = 3.5$. (d), (e), (f) OAM-CSI reconstruction results with $\epsilon_r = 3.5$, with OAM wave mode $L = 7, 9, 11$, respectively. The left and right are the real and imaginary part of the reconstruction results.

In the second example, the relative permittivity of the target increases to 4.5 as shown in Fig. 4(a). Four rectangular targets with side lengths of $\lambda/2$ are placed within the DOI, with each rectangle's boundaries spaced $\lambda/4$ apart. Fig. 4(b) and Fig. 4(c) show the reconstruction results by the use of OAM-CSI and CIE-I. Here, to improve the inversion ability, the OAM wave mode is selected as $L = 21$. However, the OAM-CSI method still fails to reconstruct the targets. Fig. 4(c) illustrates the results obtained by the CIE-I method after three rounds of optimization. The values of M_F for three rounds of optimization are 5, 7, and 10, corresponding to β values of 6, 3, and 0.5, respectively. It is shown that the CIE-I method successfully reconstructs the targets.

To verify the robustness and effectiveness of the OAM-CIE-I method, we increased the relative permittivity of targets to 5.0 and then compared the CIE-I with OAM-CIE-I methods. Fig. 5 shows the reconstruction results of these two methods. As shown in Fig. 5(a), with using the CIE-I method, it is no longer possible to accurately reconstruct the targets. However, as illustrated in Fig. 5(b), when the number of OAM electromagnetic mode is selected as $L = 11$, the OAM-CIE-I method
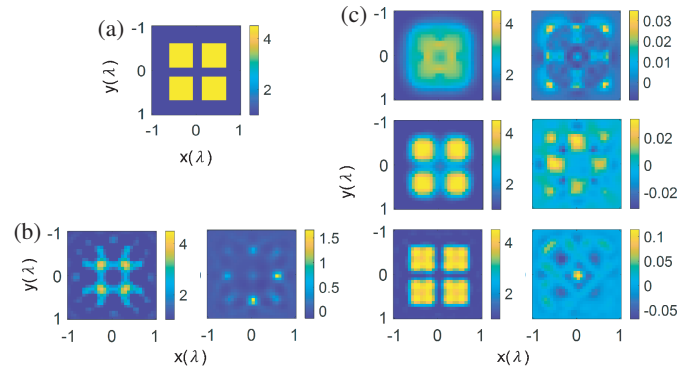

FIGURE 4. Reconstruction results obtained by OAM-CSI and CIE-I. (a) The ground truth. (b) Reconstruction results with $\epsilon_r = 4.5$ by the OAM-CSI. (c) Reconstruction results with $\epsilon_r = 4.5$ by the CIE-I for three rounds of optimization. The values of M_F for the three rounds optimization are 5, 7, and 10, coupled with β being 6, 3, and 0.5, respectively.
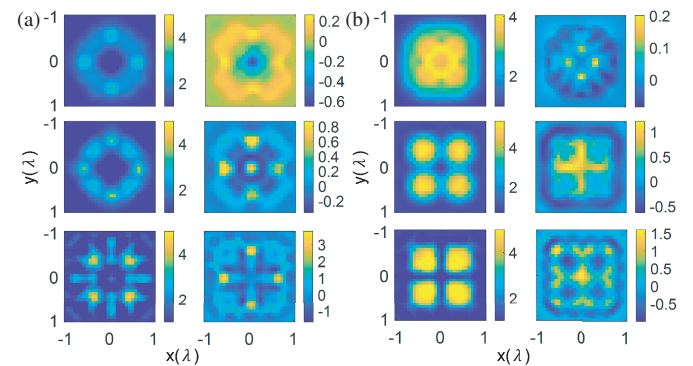

FIGURE 5. Reconstruction results obtained by CIE-I and OAM-CIE-I with $\epsilon_r = 5.0$. (a) Reconstruction results obtained by the CIE-I. (b) Reconstruction results obtained by the OAM-CIE-I. The values of M_F for the three rounds optimization are 5, 7, and 10, coupled with β being 6, 3, and 0.5, respectively. The left-hand represents the real part of the reconstruction results, while the right-hand represents the imaginary part of the reconstruction results.

can effectively reconstruct the shape and relative permittivity of the targets, achieving super-resolution imaging.

To better demonstrate the effectiveness of the OAM-CIE-I method, as shown in Fig. 6(a), the well-known "Austria" profile was chosen as the unknown target, with a grid resolution of $2\lambda/64$. Initially, the CIE-I method was employed for target reconstruction, depicted in Fig. 6(b). The CIE-I method successfully reconstructed the target with the relative permittivity of $\epsilon_r = 3.5$. However, for relative permittivity greater than 3.5, as shown in Fig. 7(a), the CIE-I method failed to reconstruct the Austria profile. As illustrated in Fig. 7(b), when the target with the relative permittivity of $\epsilon_r = 5.0$, and the number of OAM electromagnetic mode is selected as $L = 17$, the OAM-CIE-I method excels in recovering both the shape and permittivity of the target effectively.

To test the capability of the proposed OAM-CIE-I, in this example four uniform rectangular targets with $\epsilon_r = 6.0$ were selected. The synthetic data with the free noise and 10% AWGN are used for the test. The reconstruction results with the free-
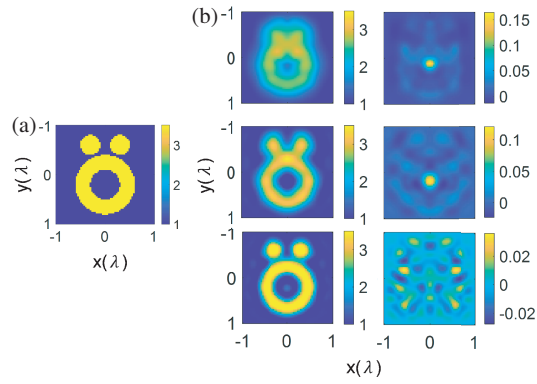
FIGURE 6. Reconstruction results obtained by CIE-I. (a) "Austria" profile. (b) Reconstruction results with $\epsilon_r = 3.5$ by the CIE-I. The values of M_F for the three rounds optimization are 5, 7, and 10, coupled with β being 6, 3, and 0.5, respectively.
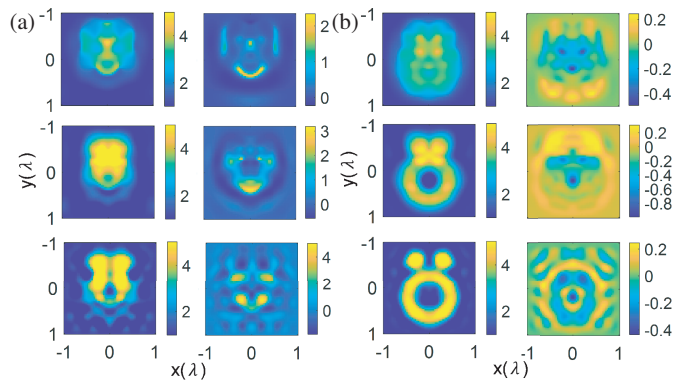

FIGURE 7. Comparison results of CIE-I and OAM-CIE-I with $\epsilon_r = 5.0$. (a) Reconstruction results obtained by the CIE-I (b) Reconstruction results obtained by the OAM-CIE-I. The values of M_F for the three rounds optimization are 5, 7, and 10, coupled with β being 6, 3, and 0.5, respectively.

noise data and 10% AWGN data after three rounds of optimization are shown in Fig. 8(a) and Fig. 8(b), respectively. It is shown that with free noise, the satisfactory reconstructed results can be obtained with the OAM electromagnetic mode selected as $L = 17$. While the 10% AWGN is added to the synthetic data, good results could also be got in spite of the presence of some artifacts in the background. The excellent results indicate that OAM-CIE-I keeps the robustness and stability and show better ability to solve quantitatively imaging of high-contrast targets.

To assess the quality of the reconstruction results, we define the relative error as follows:

$$Err^{tot} = \sqrt{\frac{1}{M}\sum_m \sum_n \left(\frac{\bar{\bar{\epsilon}}_{r;m,n}^{rec} - \bar{\bar{\epsilon}}_{r;m,n}^{true}}{\bar{\bar{\epsilon}}_{r;m,n}^{true}}\right)^2} \quad (14)$$

where $\bar{\bar{\epsilon}}_{r;m,n}^{rec}$ and $\bar{\bar{\epsilon}}_{r;m,n}^{true}$ are the reconstructed relative permittivity obtained through inversion and the actual relative permittivity, respectively. The first type of error pertains to the entire DOI Err^{tot}, while the second type concerns errors in the domain where the targets are located Err^{sct}. Table 1 shows the errors of reconstruction results from different methods.
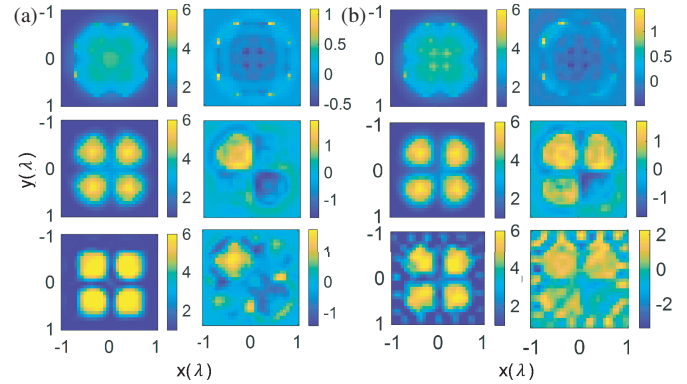

FIGURE 8. Reconstruction results obtained by the OAM-CIE-I with $\epsilon_r = 6.0$. (a) Noise free. (b) 10% noise. The values of M_F for the three rounds optimization are 5, 7, and 10, coupled with β being 6, 3, and 0.5, respectively.

TABLE 1. Reconstruction errors with different relative permittivity by CIE-I and OAM-CIE-I.

Method	ϵ_r	Target	E_{rr}^{tot}	E_{rr}^{sct}
CIE-I	3.5	Austria	0.3272	0.1655
CIE-I	4.5	Rectangle	0.4977	0.1348
OAM-CIE-I	5.0	Austria	0.6118	0.1724
OAM-CIE-I	5.0	Rectangle	0.6764	0.2147

4. CONCLUSION

This article introduces a high-contrast targets super-resolution imaging method based on orbital angular momentum (OAM-CIE-I), which combines the CIE-I model with OAM-DT method. Firstly, the initial value of the contrast function is solved using the OAM-DT method with BA, and then the initial contrast value undergoes three rounds of optimization iteration through CIE-I model. In virtue of the interaction between the OAM wave and the target, the incoherent wave information could be enhanced, and the nonlinear inversion could be fully utilized through three rounds of iterative optimization in frame of the CIE-I method. From the simulation results, it can be validated that the proposed OAM-CIE-I method could achieve better performance in terms of the capability of the solving high-contrast targets and robustness via more modes of OAM than the ones without OAM wave.

REFERENCES

[1] Chen, X., *Computational Methods for Electromagnetic Inverse Scattering*, John Wiley & Sons, 2018.

[2] Chen, Z., R. Jin, Q. Li, G. Zhao, C. Xiao, Z. Lei, and Y. Huang, "Joint inversion algorithm of sea surface temperature from microwave and infrared brightness temperature," *IEEE Transactions on Geoscience and Remote Sensing*, Vol. 60, 1–13, 2022.

[3] Yan, L., Y. Jin, C. Qi, P. Yuan, S. Wang, X. Wu, Y. Huang, and J. Chen, "Deep learning-assisted real-time forward modeling of electromagnetic logging in complex formations," *IEEE Geoscience and Remote Sensing Letters*, Vol. 19, 1–5, 2022.

[4] Soldovieri, F., F. Ahmad, and R. Solimene, "Validation of microwave tomographic inverse scattering approach via through-the-wall experiments in semicontrolled conditions," *IEEE Geoscience and Remote Sensing Letters*, Vol. 8, No. 1, 123–127, 2011.

[5] Li, B., H. Liu, Z. Zhang, and X. Gao, "A rapid microwave imaging approach for the diagnosis of traumatic brain injury," *Progress In Electromagnetics Research M*, Vol. 104, 71–80, 2021.

[6] Costanzo, S., A. Flores, and G. Buonanno, "Fast and accurate CNN-based machine learning approach for microwave medical imaging in cancer detection," *IEEE Access*, Vol. 11, 66 063–66 075, 2023.

[7] Gao, G. and C. Torres-Verdin, "High-order generalized extended born approximation for electromagnetic scattering," *IEEE Transactions on Antennas and Propagation*, Vol. 54, No. 4, 1243–1256, 2006.

[8] Li, L., H. Zheng, and F. Li, "Two-dimensional contrast source inversion method with phaseless data: TM case," *IEEE Transactions on Geoscience and Remote Sensing*, Vol. 47, No. 6, 1719–1736, 2009.

[9] Zakaria, A. and J. LoVetri, "Application of multiplicative regularization to the finite-element contrast source inversion method," *IEEE Transactions on Antennas and Propagation*, Vol. 59, No. 9, 3495–3498, 2011.

[10] Chen, W., L. Du, J. Zhao, and S. HuYan, "A Gauss-Newton inversion method based on prior back-projection information for inverse scattering problems," *Microwave and Optical Technology Letters*, Vol. 64, No. 4, 627–632, 2022.

[11] Chen, X., "Subspace-based optimization method for solving inverse-scattering problems," *IEEE Transactions on Geoscience and Remote Sensing*, Vol. 48, No. 1, 42–49, 2010.

[12] Zhong, Y., M. Lambert, D. Lesselier, and X. Chen, "A new integral equation method to solve highly nonlinear inverse scattering problems," *IEEE Transactions on Antennas and Propagation*, Vol. 64, No. 5, 1788–1799, 2016.

[13] Xu, K., L. Zhang, and Z. Wei, "Fourier bases-expansion contraction integral equation for inversion highly nonlinear inverse scattering problem," *IEEE Transactions on Microwave Theory and Techniques*, Vol. 68, No. 6, 2206–2214, 2020.

[14] Xu, B., Z. Wang, and J. He, "Beating the Rayleigh limit via aperture modulation," *Journal of Optics*, Vol. 23, No. 1, 015701, 2021.

[15] Li, L. and F. Li, "Beating the Rayleigh limit: Orbital-angular-momentum-based super-resolution diffraction tomography," *Physical Review E — Statistical, Nonlinear, and Soft Matter Physics*, Vol. 88, No. 3, 033205, 2013.

[16] Nie, P., B. Liu, P. Chen, and Y. Han, "Improved integral transform method based on gaussian kernel for image reconstruction," *IEEE Transactions on Computational Imaging*, Vol. 7, 1109–1122, 2021.

[17] Zhang, Z., S. Zheng, X. Jin, H. Chi, and X. Zhang, "Generation of plane spiral OAM waves using traveling-wave circular slot antenna," *IEEE Antennas and Wireless Propagation Letters*, Vol. 16, 8–11, 2016.

[18] Mohammadi, S. M., L. K. S. Daldorff, J. E. S. Bergman, R. L. Karlsson, B. Thide, K. Forozesh, T. D. Carozzi, and B. Isham, "Orbital angular momentum in radio — A system study," *IEEE Transactions on Antennas and Propagation*, Vol. 58, No. 2, 565–572, 2010.

[19] Li, N., L. Jiao, G. Feng, P. Li, and X. Shi, "Broadband generation orbital angular momentum beams based on uniform phase error analysis of uniform circular array," *Progress In Electromagnetics Research Letters*, Vol. 120, 53–58, 2024.